Meteor Head Echo Analyses from Concurrent Radar Observations at AMISR Resolute Bay, Jicamarca, and Millstone Hill

T. Hedges[1], N. Lee[1], and S. Elschot[1].

[1]Department of Aeronautics and Astronautics, Stanford University, Stanford, CA, USA

Key Points:

- Sensitivity to head echoes of three high-power radar instruments across varying latitudes are studied via concurrent observations
- An inter-pulse phase-matching technique enables accurate range deceleration measurements
- When radar beam is zenith-pointing, higher decelerations are observed at lower altitudes, reflecting the atmospheric neutral density profile

Corresponding author: Trevor Hedges, `thedges@stanford.edu`

Abstract

On October 10th and 11th, 2019, high-power radar observations were performed simultaneously for eight hours at Resolute Bay Incoherent Scatter North (RISR-N), Jicamarca Radio Observatory (JRO), and Millstone Hill Observatory (MHO). The concurrent observations eliminate diurnal, seasonal, and space weather biases in the meteor head echo populations and elucidate relative sensitivities of each facility and configuration. Each facility observed thousands of head echoes, with JRO observing tens of thousands. An inter-pulse phase matching technique employs Doppler shifts to determine head echo range rates (velocity component along radar beam) with order-of-magnitude greater accuracy versus measuring the Doppler shift at individual pulses, and this technique yields accurate range rates and decelerations for a subset of the head echo population at each facility. Because RISR-N is at high latitude and points away from the ecliptic plane, it does not observe head echoes with range rates faster than 55 km/s, although its head echo population demonstrates a bias toward larger and faster head echoes. At JRO near the equator, a larger spread of range rates is observed. MHO observes a large spread of range rates at mid-latitude despite its comparable frequency to RISR-N, but this occurs because its beam was pointed at a 45° elevation angle unlike RISR-N and JRO which were pointed near-zenith. A trend of greater decelerations at lower altitudes is observed at RISR-N and JRO, with decelerations of up to 60 km/s^2, but high-deceleration events of up to 1000 km/s^2 previously observed in head echo studies are not observed.

1 Introduction

Researchers frequently use high-power large aperture (HPLA) incoherent scatter radar (ISR) instruments around the world to gather data about meteoroids entering Earth's atmosphere. HPLA radar instruments measure between hundreds and thousands of head echoes per hour, depending on factors including frequency, power, geographic location and beam direction, in addition to the observed meteor population, that influence head echo detectability. High detection rates enable the use of statistical methods for head echo populations. The observed head echoes often originate from particles that are tens of microns in diameter; larger than the particles that can be observed in situ via impact detectors (Baggaley et al., 2007), but smaller than those observed via optical methods (Brown et al., 2017) (Campbell-Brown & Close, 2007). Furthermore, signal processing techniques can be leveraged to obtain extremely accurate measurements of meteor motion during atmospheric entry from radar data.

As a meteoroid ablates in Earth's atmosphere, a plasma forms at altitudes from 80 to 130 kilometers due to sputtering and thermal ablation upon high-velocity collisions between the meteoroid and atmospheric molecules (Popova et al., 2001) (Guttormsen et al., 2020). The high-density plasma cap that surrounds the meteoroid reflects radio waves, producing the head echo radar signature. Head echoes are observable at any HPLA radar. As the plasma expands and undergoes collisions with the surrounding atmosphere, a Farley-Buneman gradient-drift instability may develop in the meteor trail and create a non-specular radar return (Oppenheim & Dimant, 2015) (Oppenheim et al., 2000). Most trails occur at equatorial radars due to field-aligned-irregularity (FAI) scattering when the incident wave is perpendicular to the background magnetic field (L. P. Dyrud et al., 2005), although non-FAI scattering has also been observed at higher latitudes (Kozlovsky et al., 2020) (Chau et al., 2014).

As the meteoroid heats and ablates, differential ablation may occur where certain constituents thermalize before others. This can create variation in radar cross-section during head echo detection, and such variation at the Arecibo radar facility was demonstrated to match the results of an ablation model (L. Dyrud & Janches, 2008) (Janches et al., 2009). The effect has been observed in the laboratory for submicron-scale particles (DeLuca et al., 2022). The process of differential ablation may cause the meteoroid to fragment during atmospheric entry. Fragmentation has been observed optically (Vida et al., 2021), and on radar instruments via polarization of the head echo radar return (Close et al., 2011) or via interference patterns in the head echo (Gao & Mathews, 2015). The presence of differential ablation and fragmentation motivate further investigation of meteor plasma dynamics and scattering.

An analytical model of meteor head echo scattering was formulated (Close et al., 2004), providing a relationship between the strength of a radar return throughout its detection and initial meteoroid mass (Close et al., 2005). Initial plasma simulation efforts used a two-dimensional domain to model the meteor head echo plasma density. The density is fed into an electromagnetics scattering simulation to validate the analytical scattering model and relax assumptions (L. P. Dyrud et al., 2008a) (L. P. Dyrud et al., 2008b). Scattering simulation also verifies the polarization effects that occur during a fragmentation event observed via radar (Vertatschitsch et al., 2011). The scattering simulations were later extended to three dimensions (Marshall & Close, 2015). More recent work uses three-dimensional plasma simulations to determine the most physically accurate meteor plasma density profile to date (Sugar et al., 2018) (Sugar et al., 2019), and then uses the simulated density as input to a three-dimensional scattering simulation (Sugar et al., 2021). The initial analytic and numerical models assumed the plasma density profile is Gaussian, but multi-frequency radar observations imply that the profile is more like $1/r^2$, where r is the distance from the meteoroid center (Marshall et al., 2017). These observations are supported by the three-dimensional plasma simulations. The theoretical and simulated scattering properties of meteors enables relationships between the strength of a radar return over its detection and initial meteoroid mass to be formulated (Close et al., 2005), and this has furthermore been tied to meteoroid bulk density (Drew et al., 2004) (Close et al., 2012).

Head echo observations also serve as a probe of the upper atmosphere in regions above where weather balloons can take measurements, but below where the effect of atmospheric drag on satellites in low-Earth orbit can be observed (A. Li & Close, 2015). The deceleration of a head echo is closely related to the neutral atmospheric density, in addition to the parent meteoroid ballistic parameter and mass loss rates, so models that capture these dynamics can predict lower thermospheric atmospheric density as a function of altitude. Techniques are available to determine neutral densities as a function of altitude using bulk observations of head echo velocities and decelerations (A. Li & Close, 2016), and also via individual head echo observations (Limonta et al., 2020).

Properties of head echoes that are observed via radar include signal strength, altitude, range rate, and range deceleration. The range rate is the component of head echo velocity along the radar beam, and range deceleration is the time derivative of range rate. Comparative studies of head echo populations to assess the sensitivities of various radars have been performed. One such study presents head echo populations from Arecibo Observatory, the AMISR Poker Flat Incoherent Scatter Radar (PFISR), and Sondrestrom Research Facility (SRF), including head echo decelerations along the radar beams (Mathews et al., 2008). It is known that the Arecibo Observatory HPLA radar is capable of detecting some of the smallest meteors (less than 1 μg) compared to other facilities (Janches et al., 2008). The Millstone Hill Observatory radar instrument is also capable of observing head echo populations (Erickson et al., 2001).

In October of 2019, a meteor radar data collect was performed concurrently for eight hours total at three radar facilities, including Resolute Bay ISR (RISR-N), the Millstone Hill ISR at MIT Haystack Observatory (MHO), and Jicamarca Radio Observatory (JRO), with the intent to study latitudinal variation in the neutral atmosphere via meteor observations at varying latitudes but similar longitudes. Since each facility is unique in its operation and location, understanding the observation biases of each radar is essential to understanding meteors and the atmosphere. Biases inherent to latitude include the beam orientation and its angle relative to meteoroid sources, varying geomagnetic field orientation and ionospheric conditions. Other biases can result from the radar carrier frequency, incident power (Urbina & Briczinski, 2011), beam pattern, incident polarization, and local solar time. The results of this experiment are summarized and the effect of the biases at each facility and configuration are presented.

This paper is structured as follows: we first discuss the radar experiment parameters and methods utilized to improve measurement accuracy, including an inter-pulse phase matching technique, how its use differs between facilities, and the uncertainty that remains in the resulting head echo range rate and deceleration measurements. We then present observations of the head echo populations at each facility, discuss factors that influence variations between them, compare the results with previous meteor head echo observations, and discuss the implications of the results. We conclude with a summary of our findings and our future plans for this dataset.

2 Experimental Method

The meteor radar observations at each facility utilize long phase-coded pulses to maximize transmitted power and hence sensitivity. Such pulses leverage the sparsity of head echo radar signatures, where there is typically only a single scattering target, the head echo of interest, being observed at a given time (Volz & Close, 2012). Matched filters are applied to the raw data to minimize range ambiguity. A downside to this approach is that the autocorrelation functions of long pulse codes contain range sidelobes, which appear in the data for stronger head echoes. However, since it is uncommon for the radar returns of two separate head echoes to overlap, the main lobe clearly indicates head echo range and sidelobes do not prove problematic.

2.1 Experiment Parameters

At RISR-N and JRO, a minimum-sidelobe 51-baud (MSB 51) code of duration 51 μs is used to maximize head echo signal returns. The radar beams at JRO and RISR-N were pointed almost directly upward to minimize beam range required to reach the altitude range of 80-120 km where meteors are observed (A. Li & Close, 2016). At MHO, a Barker-7 code of length 42 μs is used to produce nearly comparable signal-to-noise (SNR) performance without any compromise on code fidelity, since at the time of experiment, the facility was not capable of the shorter 1 μs baud length used at RISR-N and JRO. The MHO radar beam was pointed at a 45 degree elevation due West to keep the meteor altitude range away from ground clutter present in the region. Each facility utilizes an inter-pulse period (IPP) of 2 milliseconds or less to maximize pulses and improve range deceleration measurement of head echoes. Experiment parameters and details for each radar facility are provided in Table 1.

The dynamics of meteoroid ablation and the resulting head echoes are dependent on the conditions of the lower thermospheric neutral atmosphere and ionosphere at the time of experiment. Table 2 specifies the solar and geomagnetic indices for the dates and times of experiment.

2.2 Signal Processing Techniques

A Doppler shifted matched filter bank was utilized to detect head echos. The Doppler shift of a head echo is directly proportional to the range rate, so by maximizing the SNR versus Doppler shift at each pulse and within the range that a head echo is present, a coarse range rate profile versus time is determined. This technique is one such method widely used to determine head echo range rates in time, but the resulting profiles contain too much noise to be useful for quantifying range deceleration. Similarly, one could determine the range rate of a head echo by fitting a curve to the range gates of maximum signal return versus time, but in practice this technique only yields an average range

Table 1. Parameters for each radar facility and experimental configuration.

Parameter	RISR-N	MHO	JRO	Units
Longitude	−94.91	−72.47	−76.87	deg
Latitude	74.73	44.16	−11.95	deg
Observation date	Oct. 10-11, 17-18	Oct. 10-11	Oct. 10-11	–
Observation time	09:00-13:00	09:00-13:00	05:00-13:00	UTC
Beam Azimuth	26	270	–	deg
Beam Elevation	86	45	90	deg
Carrier Frequency	442.5	442.9	49.9	MHz
Pulse Code	MSB 51	Barker 7	MSB 51	–
Transmit Power (peak)	2	2	6	MW
Baud Rate	1	6	1	μs
Inter-pulse Period	1.4	2.0	1.25	ms
Sample Rate	2	1	1	MHz

Table 2. Solar and geomagnetic indices on the experiment dates and times. The low F10.7 values reflect the solar minimum at the time of experiment, and the low values of K_p and A_p reflect a quiet geomagnetic day (Matzka et al., 2021).

Index	Oct. 10, 2019			Oct. 11, 2019		
Time (UTC)	09-12	12-15	Full-day average	09-12	12-15	Full-day average
K_p	2.00	1.33	2.42	2.00	1.33	1.71
A_p	7	5	13.4	7	5	6.9
$F_{10.7}$	–	–	67.5	–	–	68.5

rate, and does not produce accurate results for range deceleration. Therefore, we must employ additional information to more accurately pinpoint range rate: the phase difference between subsequent pulses. In practice, this technique, henceforth referred to as *inter-pulse phase matching*, produces significantly smoother range rate profiles.

2.2.1 Inter-Pulse Phase Matching

The inter-pulse phase-matching technique is employed to yield order-of-magnitude increase in range rate accuracy versus simply utilizing Doppler shifts from individual pulse returns. This enables range deceleration measurements via curve fitting of range rates. Comparison of range rate profiles with and without this method for a well-behaved head echo at RISR-N is shown in Figure 1.

An initial guess for the average head echo range rate is required to apply a Doppler shifted matched filter to the raw data. This is determined by taking the average range rate of the coarse range rate profile, weighted by the SNR. Then, the phase-matching technique measures Doppler shift via phase difference between consecutive pulses at the range gates of maximum signal return. The relationship between range rate and phase difference for coded pulses, neglecting phase aliasing, is

$$\Delta\phi = \frac{4\pi f_0 T v}{c}, \quad (1)$$

where f_0 is the carrier frequency, T is the IPP, v is the Doppler velocity (observed range rate), and c is the speed of light (Loveland et al., 2011) (Skolnik, 2008). This expression is not readily useful since $\Delta\phi$ may be very large; for a RISR-N or MHO head echo with range rate of 50 km/s, $\Delta\phi \approx 1300$ rad. However, taking a second difference of phase

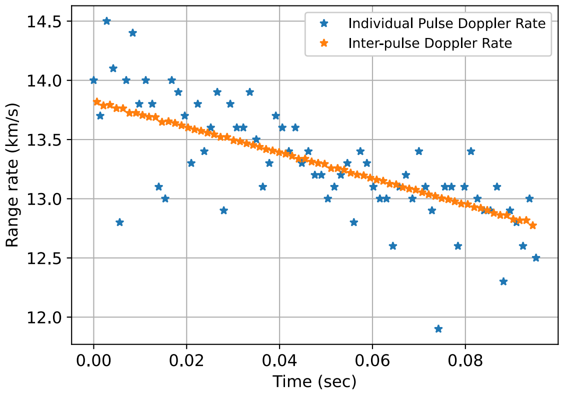

Figure 1. Range rate for a head echo at RISR-N obtained via the inter-pulse phase-matching technique, which utilizes the phase difference between pulses to obtain a more accurate range rate profile, versus Doppler shift measurement at each individual pulse.

between consecutive pulses via a finite difference of Eq. 1 yields an expression for Δv, the change in head echo range rate between pulses, which is small for a head echo between consecutive pulses with the short IPPs used in this experiment. Physically, the second difference of phase measures the change in Doppler shift between consecutive pulses across the head echo lifetime, which directly relates to the deceleration along the radar beam. Accounting for phase aliasing, the second difference of phase is

$$\Delta^2\phi = \mathrm{mod}\left(\frac{4\pi f_0 T \Delta v}{c}, 2\pi\right), \tag{2}$$

and for a RISR-N or MHO head echo that decelerates such that $|\Delta v| = 25$ m/s between pulses, this gives $|\Delta^2\phi| \approx 0.65$ rad. It is therefore possible to remove discontinuities in the profile of $\Delta\phi$ that arise due to phase aliasing, as demonstrated in Figure 2. This procedure is known as *phase unwrapping*. If Δv is large enough, aliasing due to the modulo may cause $\Delta^2\phi$ to appear smaller than it really is; this is effectively only a concern at RISR-N and MHO due to their high carrier frequency. This possibility can be assessed by adding -2π (or any multiple of concern) to the result for $\Delta^2\phi$, and comparing the slope of the resulting range rate to the coarse range rate. Since $\Delta^2\phi$ is proportional to f_0 and T, radar instruments with higher carrier frequencies or longer IPPs will have a steeper $\Delta\phi$ profile with more discontinuities. The net result of the higher carrier frequency at RISR-N and MHO, but comparable IPP at all three facilities, is for many RISR-N and MHO head echoes to have ten or more $\Delta\phi$ discontinuities, whereas JRO head echoes usually contain at most two discontinuities. Furthermore, the proportionality of $\Delta^2\phi$ to Δv causes head echoes with higher range decelerations to have a steeper $\Delta\phi$ profile.

A technique to unwrap the discontinuous $\Delta\phi$ signal is to determine where $\Delta\phi$ varies by more than π between pulses. This is accurate for almost all head echoes at JRO due to the slow variation of $\Delta\phi$. At RISR-N and MHO, variations of $\Delta\phi$ greater than π can naturally occur due to noise despite lack of a discontinuity, causing the technique to fail. In nearly all such cases, the $\Delta\phi$ profile can be manually corrected via inspection.

The range rate profile obtained via this algorithm and Eq. 1 will henceforth be referred to as the *phase-difference range rate* profile. Since the phase unwrapping algorithm is equivalent to integrating Eq. 2, the resulting velocity profile does not include a constant of integration, v_0, which is the largest source of uncertainty in this method. To find v_0 at RISR-N and MHO, the coarse range rate is accurate enough that a least-squares fit between this profile and the smooth unwrapped profile can be performed with v_0 as

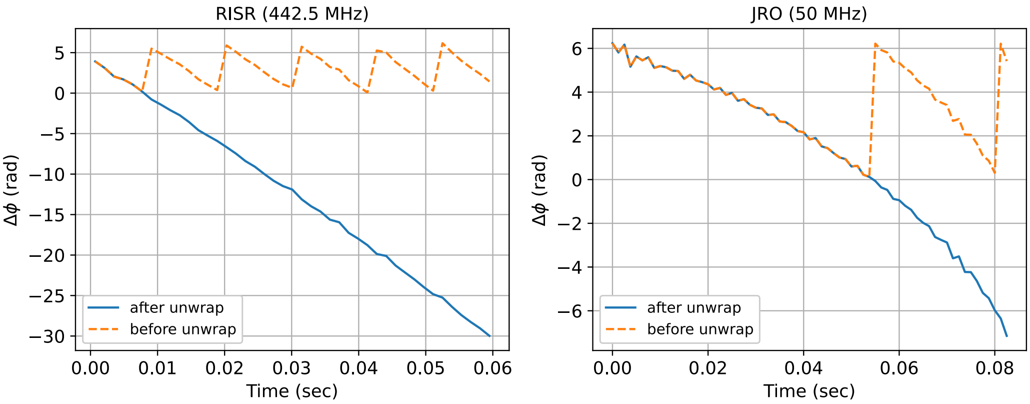

Figure 2. $\Delta\phi$ for head echoes near 50 km/s at RISR-N and JRO before and after removal of modulo discontinuities.

a parameter. At JRO, due to the lower carrier frequency, the coarse range rate profile is too noisy for this approach to be reasonable, so v_0 is determined by setting the average range rate from an exponential fit to the maximum-SNR range gates equal to the mean value of the phase-difference range rate.

In the phase-difference range rate profiles obtained at JRO, ripples occur due to discrete changes in the range gate at which the complex matched-filter signal is sampled (Galindo et al., 2013). To mitigate this, the signal is linearly interpolated between range gates using the aforementioned exponential range fit before taking the phase difference between consecutive pulses. This approach did not prove useful at the other facilities.

2.2.2 Determination of Range Decelerations

Since the magnitude of noise renders finite-differencing of the phase-difference range rate profile infeasible, range decelerations are determined via an exponential least-squares curve fit to the range rate versus time, as depicted in Figure 3 for a strong head echo and a weak head echo at JRO. The exponential fit is parameterized by the function

$$v_{fit}(t) = a + be^{\lambda t}, \tag{3}$$

with parameters a, b, and λ. The time derivative of this fit provides a range deceleration estimate over the detection interval of the meteor. Accuracy of the measured range rate and deceleration can vary based on the head echo, due to SNR of the head echo itself, success of the phase unwrapping algorithm, and presence of other plasmas or clutter. The r^2 value of the exponential fit serves as an indicator of measurement accuracy of a particular head echo. The 95% confidence interval provides an estimate of uncertainty in the range rate fit. Furthermore, we compute confidence intervals for the range deceleration via the covariance transform

$$\sigma_{\dot{v}_r}^2 = J_1 \Sigma J_1^T, \tag{4}$$

$$J_1 = \left[\frac{\partial v_{fit}}{\partial a}, \frac{\partial v_{fit}}{\partial b}, \frac{\partial v_{fit}}{\partial \lambda} \right]^T, \tag{5}$$

where Σ is the covariance matrix estimated by the curve fit routine for the exponential fit parameters. The 95% confidence interval is related to the range rate variance as

$$\epsilon_{\dot{v}_r} = 4\sigma_{\dot{v}_r}.$$

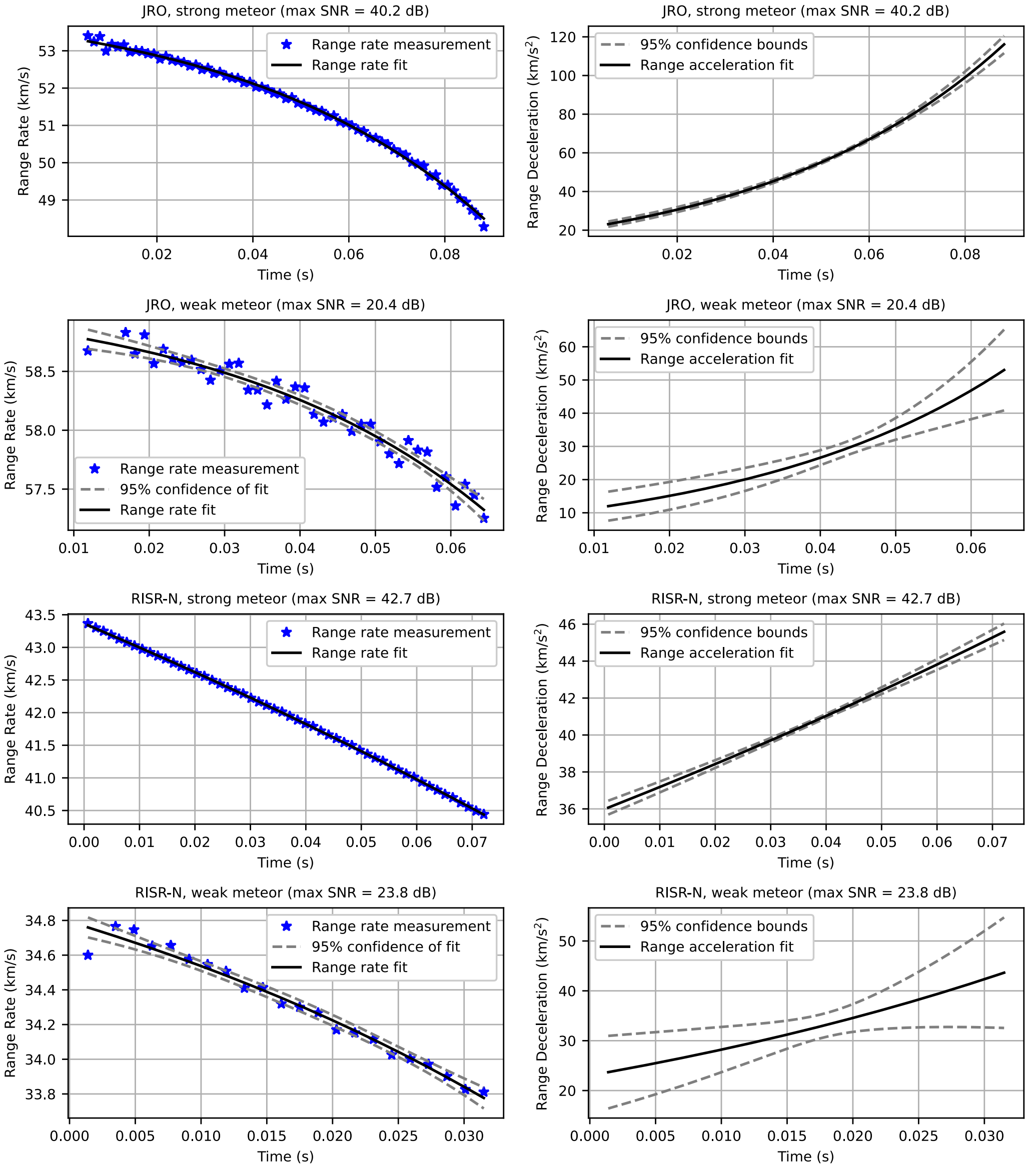

Figure 3. Range rate (left) and range deceleration (right) profiles via phase-differencing for strong and weak head echoes observed at RISR-N and JRO. The strong echoes have max SNR greater than 40 dB, and weak echoes no greater than 24 dB.

3 Population Analysis and Discussion

Since all three facilities recorded data from 09:00-13:00 UTC on October 10th and 11th, the head echo populations from these timespans can be directly compared to reveal insights on how each instrument and its observations differ, without conflating these insights with atmospheric variation due to diurnal, seasonal, and solar cycle effects. Initial detection of head echos is performed via inspection of data with a Doppler-shifted matched filter bank.

The head echo detection rates for each facility throughout the concurrent data collect are compared in Figure 4. The rates at RISR-N and MHO remain relatively constant throughout the experiment duration, owing to the lack of cluttering phenomena. Almost no such phenomena besides that of satellites are observed at RISR-N, and the sporadic E events observed at MHO are not strong enough to significantly obscure head echoes. Conversely, the rates at JRO vary due to the presence of range-aliased spread F events that obscure head echoes, and decay to near-zero as the equatorial electrojet becomes prominent after sunrise.

Overall, the configuration at JRO is significantly more sensitive to head echos than the other facilities, with maximum detection rate of more than 80 meteors per minute. This results from its lower carrier frequency capable of detecting less dense plasma, and hence smaller meteors. This rate is higher than the peak rate of 50 meteors per minute observed in a previous experiment at JRO by Chau and Woodman (2004), which can be attributed to use of the more sensitive MSL 51 pulse instead of Barker-13 as in the previous experiment. Despite RISR-N and MHO operating at the same frequency, the configuration at MHO is more sensitive to head echoes than RISR-N, which likely results from its lower latitude and smaller angle between its beam and the ecliptic plane. The use of the Barker-7 pulse code, despite containing fewer bauds than the MSB 51 code and thus yielding reduced SNR, is not a significant hindrance to head echo detection rates. The detection rate at MHO is consistent with a prior meteor experiment by Erickson et al. (2001) in which peak rates of up to 7 meteors per minute were observed before dawn using a Barker-13 coded pulse. The rate at RISR-N is consistent with the peak rate of 2.7 meteors per minute previously observed at the similar PFISR facility (Sparks et al., 2009).

An additional factor that potentially contributes to detection rates is the longitude variation between facilities, the largest of which is 22.4 degrees between RISR-N and MHO. JRO and MHO are closer in longitude, with only 4.4 degrees of longitudinal separation. Therefore, RISR-N is effectively positioned such that its local time lags that of the other facilities by about 90 minutes. Previous observations observe a clear peak in the head echo detection rate at dawn (Y. Li & Zhou, 2019). Since these observations occur at dawn, and no clear peak or trend is visible in the detection rate at any facility, it can be assumed that 90 minutes does not make a significant difference compared to the other factors.

A subset of the population at each facility is manually selected for further analysis. This subset is not exhaustive, but contains a consistent spread of head echos across the duration of the concurrent data collect, with at least 300 head echoes at each facility. To ensure the measured range rates and range decelerations of these head echoes are accurate, only head echoes with sufficiently high r^2 values in their exponential range rate versus time fits are included in the subset. The threshold r^2 value at RISR-N and MHO is 0.99, and at JRO is 0.90. The lower value at JRO was chosen since the lower carrier frequency, and therefore more gradual inter-pulse phase change due to the Doppler shift, produces noisier phase-difference range rate profiles. Since the phase unwrap algorithm is less likely to fail with the more gradual overall phase change, many fits with lower r^2 values are still accurate at JRO despite the noise. The altitudes and range rates of the subset of head echoes selected for further analysis at each facility are plotted in Figure 5

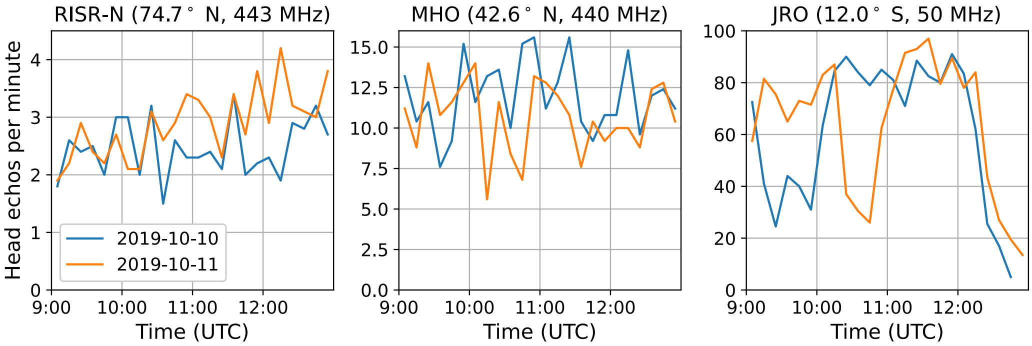

Figure 4. Detection rate of head echoes throughout concurrent observation at RISR-N, JRO, and MHO.

to demonstrate the sensitivity and observation biases of each facility. Range decelerations are indicated via point color. To more clearly demonstrate head echo range rate sensitivities, Figure 6 depicts the cumulative distribution of range rate at specific altitude ranges at each facility.

The head echo distributions in altitude and range rate are different at each facility because each beam points in a different direction relative to the incoming meteor population. Since each facility only observes the component of velocity along its beam, each facility effectively observes the incoming meteor population from a different perspective. At JRO and MHO, there is the expected trend of faster head echoes at higher altitudes, which is readily visible in Figure 6. This trend is not observed in the RISR-N population. Furthermore, RISR-N has a clear range rate cutoff at 55 km/s. Both of these effects are likely due to its high-latitude location, and thus the large angle between the beam boresight and the solar ecliptic plane where most meteoroids travel. The resulting effect is that nearly all meteors contain a significant component of horizontal velocity through the beam, and because RISR-N does not have interferometric capability, this component is not detected. Assuming the meteoroids do not originate from outside the solar system or encounter third-body perturbations, their combined velocity cannot exceed 72.8 km/s, which includes the unknown horizontal velocity. The aforementioned local time variation of RISR-N with respect to the other facilities may slightly influence its observed range rate distribution, but given the 2.5 hours of local time overlap between the facilities, which is a majority of the experiment duration, this effect can be assumed insignificant compared to the latitudinal effect. There is also a large population of meteors at RISR-N with velocities between 40 km/s and 55 km/s, since such meteors generate a higher-density plasma that is detectable via the higher carrier frequency. The head echo population at JRO is more consistently spread across range rates, owing to its equatorial location and ability to detect smaller and slower meteors.

Above 35 km/s, the populations at RISR-N and JRO demonstrate a clear trend of observing higher decelerations at lower altitudes, as expected given larger drag where the atmosphere is denser. Although head echo deceleration is also dependent on factors such as the ballistic parameter, which is expected to decrease across the lifetime of a meteoroid and enhance deceleration, the overall trend across hundreds of meteor observations is clearly indicative of atmospheric density variation. This trend is not observed at MHO due to its beam elevation 45° due west. Since every incoming meteoroid has some vertical component of velocity and deceleration, when the beam is zenith-pointing, some positive range rate and deceleration will be observed. At MHO, a meteor entering due west at 45° from the horizontal will cross the beam at a right angle, such that

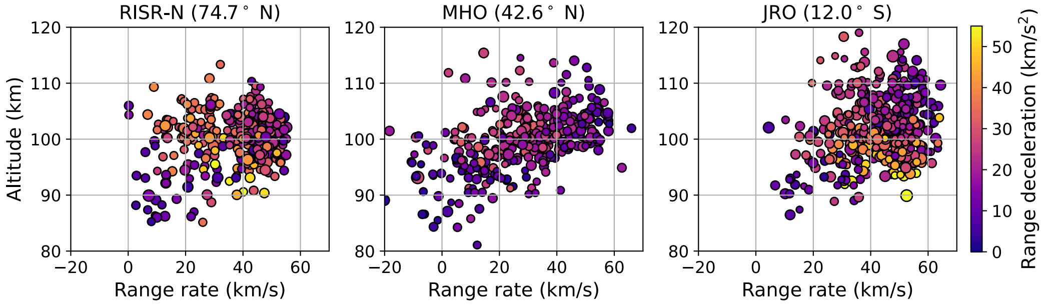

Figure 5. Scatter plot of head echo range vs range rate detected at the three facilities. Each point is color-coded by observed range deceleration, and sized by maximum SNR of the head echo.

zero range rate and deceleration is observed. If the meteor has high horizontal velocity due west, its velocity vector will have a component pointed away from MHO rather than toward MHO, such that negative range rate is observed. This effect broadens the overall spread of meteor range rates on the low end, with a small fraction below zero.

The overall magnitude of decelerations in the range of tens of kilometers per second squared is in general agreement with the results from the Arecibo radar presented in a comparative head echo study by Mathews et al. (2008). Most head echoes at Arecibo exhibit decelerations of up to about 150 km/s^2; larger than is observed in this experiment, but this is justified given the relative sensitivity of Arecibo to very small meteors (Janches et al., 2008) which decelerate faster. However, Mathews et al. also presents data from the PFISR and SRF radar instruments, in which a small fraction of head echoes at PFISR and a majority at SRF exhibit extremely high decelerations in the hundreds of kilometers per second squared, which is not observed in the populations presented at RISR-N, JRO, or MHO. Since Mathews et al. does not specify how deceleration is measured, it is possible that the maximum decelerations within each head echo were used, unlike our analysis which determines the decelerations at maximum signal strength. This would create a bias toward larger values, but almost certainly does not explain an order-of-magnitude difference. The difference could result from a radar sensitivity effect; one plausible physical explanation is that PFISR and SRF observe fragmentation events where individual fragments decelerate fast while collectively generating a large enough radar signature to be observed. This remains inconsistent with the lack of such observations at RISR-N in this experiment, as the PFISR experiment utilized a similar carrier frequency, pulse length and IPP. Therefore, further investigation into this discrepancy is necessary.

4 Conclusions and Future Work

In this paper, the ability of a phase-matching technique for coded pulses to substantially and consistently increase accuracy of measured head echo range rate is demonstrated. The technique is applied to data collected from a concurrent HPLA meteor radar experiment at the RISR-N, JRO, and MHO facilities at varying latitudes and similar longitudes. Although the phase-matching technique is sensitive to facility and experiment parameters including inter-pulse period and carrier frequency, and must be tailored slightly to these variations, it can be employed at any HPLA radar facility capable of inter-pulse periods on the order of milliseconds. By taking exponential curve fits, decelerations and their uncertainties are quantifiable, and it is shown that these uncertainties are generally acceptable for many head echoes. Since head echo deceleration depends heavily on

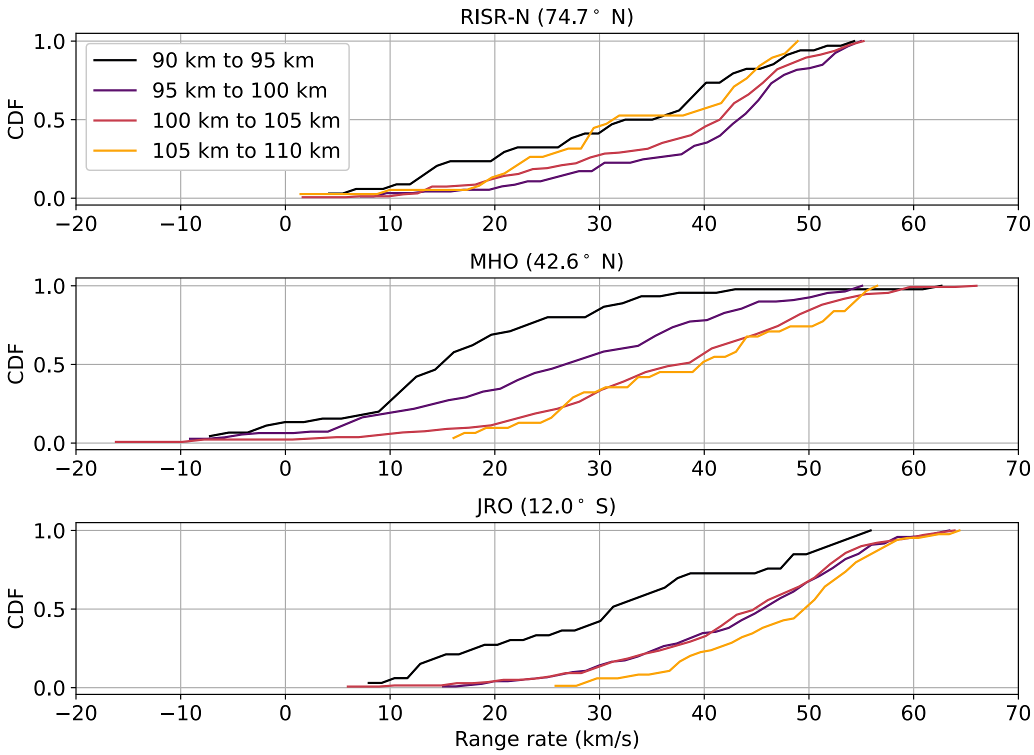

Figure 6. Cumulative distribution function of head echo population range rate within specified altitude ranges at each facility.

atmospheric neutral density, having a proven method that quantifies deceleration is essential progress toward enabling measurement of atmospheric neutral densities at any HPLA radar facility.

A comparison of the head echo populations observed by RISR-N, JRO, and MHO demonstrates that the JRO is overall most sensitive to head echoes as a result of its lower carrier frequency. Despite RISR-N and MHO operating at the same frequency, MHO observes more meteors, indicating that the latitude and beam angle relative to the ecliptic plane is a significant factor in meteor detectability. In general, the detection rates at each facility are consistent with before-dawn observations from previous experiments. The use of longer MSB codes instead of Barker codes produces a sensitivity increase from previous experiments in some cases. The overall detectability of a head echo is a combination of radar parameters such as beam direction, location, local time, frequency, and polarization, and meteoroid parameters including entry velocity, mass, and density. We will continue to investigate head echo detectability, and how radar observation biases can be removed to best understand the meteoroids themselves. Since many more head echoes exist in the data, a future publication will analyze a larger sample of head echoes, enabling the discussion of changes in the head echo population during the experiment that result from local time variation or variations in the neutral atmosphere.

Since three-dimensional velocities are currently unavailable at RISR-N and MHO, the analysis focuses on range rates and range decelerations. However, full velocities will be obtained at JRO via interferometric data for a more comprehensive quantification of its head echo population. This information will also be used to propagate the possible meteoroid orbits backward in time to further understand their possible origins within the solar system. At RISR-N, future work will estimate the horizontal component of head echo velocity. The results from RISR-N and JRO exhibit a trend of higher decelerations at lower altitudes at range rates greater than 35 km/s. This demonstrates that meteor head echo populations can be used as a probe of lower thermospheric neutral density where the radar beam is zenith-pointing, and so lower thermospheric neutral densities as a function of altitude will be estimated via populations from these two facilities, and better understand latitudinal coupling of neutral densities.

Data Availability Statement

The head echo detection rates and raw data for each head echo presented in this work are archived at `https://doi.org/10.5281/zenodo.6589243`, licensed under the Creative Commons Attribution 4.0 International license (Hedges et al., 2022).

Acknowledgments
The authors graciously thank those that provided assistance with data collection: Marco Milla and Karim Kuyang Ruiz with Jicamarca, Phil Erickson and Ryan Volz with Millstone Hill, and Roger Varney with Resolute Bay. Thanks also to Meers Oppenheim and Glenn Sugar for their advice with data analysis and signal processing, and Jared Blanchard for his advice for statistics and uncertainty quantification. This work was funded by NSF Grant AGS-1920383, and student funding was supplemented by NSF Grant AGS-2048349.

References

Baggaley, W. J., Marsh, S. H., & Close, S. (2007). Interstellar meteors. *Dust in Planetary Systems*, *ESA SP-643*.

Brown, P., Stober, G., Schult, C., Krzeminski, Z., Cooke, W., & Chau, J. L. (2017). Simultaneous optical and meteor head echo measurements using the Middle Atmosphere Alomar Radar System (MAARSY): Data collection and preliminary analysis. *Planetary and Space Science*, *141*, 25–34. doi: 10.1016/j.pss.2017.04.013

Campbell-Brown, M. D., & Close, S. (2007). Meteoroid structure from radar head echoes. *Monthly Notices of the Royal Astronomical Society*, *382*(3), 1309–1316. doi: 10.1111/j.1365-2966.2007.12471.x

Chau, J. L., Strelnikova, I., Schult, C., Oppenheim, M. M., Kelley, M. C., Stober, G., & Singer, W. (2014). Nonspecular meteor trails from non-field-aligned irregularities: Can they be explained by presence of charged meteor dust? *Geophysical Research Letters*, *41*(10), 3336–3343. doi: 10.1002/2014GL059922

Chau, J. L., & Woodman, R. F. (2004). Observations of meteor-head echoes using the Jicamarca 50 MHz radar in interferometer mode. *Atmospheric Chemistry and Physics*, *4*, 511–521.

Close, S., Kelley, M., Vertatschitsch, L., Colestock, P., Oppenheim, M., & Yee, J. (2011). Polarization and scattering of a long-duration meteor trail. *Journal of Geophysical Research: Space Physics*, *116*, A01309. doi: 10.1029/2010JA015968

Close, S., Oppenheim, M., Durand, D., & Dyrud, L. (2005). A new method for determining meteoroid mass from head echo data. *Journal of Geophysical Research: Space Physics*, *110*, A09308. doi: 10.1029/2004JA010950

Close, S., Oppenheim, M., Hunt, S., & Coster, A. (2004). A technique for calculating meteor plasma density and meteoroid mass from radar head echo scattering. *Icarus*, *168*, 43–52. doi: 10.1016/j.icarus.2003.11.018

Close, S., Volz, R., Loveland, R., Macdonell, A., Colestock, P., Linscott, I., & Oppenheim, M. (2012). Determining meteoroid bulk densities using a plasma scattering model with high-power large-aperture radar data. *Icarus*, *221*, 300–309. doi: 10.1016/j.icarus.2012.07.033

DeLuca, M., Sternovsky, Z., Armes, S. P., Fielding, L. A., Horányi, M., Janches, D., ... Plane, J. M. C. (2022). Differential Ablation of Organic Coatings From Micrometeoroids Simulated in the Laboratory. *Journal of Geophysical Research: Planets*, *127*. doi: 10.1029/2021JE007168

Drew, K., Brown, P. G., Close, S., & Durand, D. (2004). Meteoroid bulk density determination using radar head echo observations. *Earth, Moon, and Planets*, *95*, 639–645. doi: 10.1007/s11038-005-2246-2

Dyrud, L., & Janches, D. (2008). Modeling the meteor head echo using Arecibo radar observations. *Journal of Atmospheric and Solar-Terrestrial Physics*, *70*, 1621–1632. doi: 10.1016/j.jastp.2008.06.016

Dyrud, L. P., Ray, L., Oppenheim, M., Close, S., & Denney, K. (2005). Modelling high-power large-aperture radar meteor trails. *Journal of Atmospheric and Solar-Terrestrial Physics*, *67*, 1171–1177. doi: 10.1016/j.jastp.2005.06.016

Dyrud, L. P., Wilson, D., Boerve, S., Trulsen, J., Pecseli, H., Close, S., ... Lee, Y. (2008a). Plasma and electromagnetic simulations of meteor head echo radar reflections. *Earth, Moon and Planets*, *102*(1-4), 383–394. doi: 10.1007/s11038-007-9189-8

Dyrud, L. P., Wilson, D., Boerve, S., Trulsen, J., Pecseli, H., Close, S., ... Lee, Y. (2008b). Plasma and electromagnetic wave simulations of meteors. *Advances in Space Research*, *42*, 136–142. doi: 10.1016/j.asr.2007.03.048

Erickson, P. J., Lind, F. D., Wendelken, S. M., & Faubert, M. A. (2001). Meteor Head Echo Observations Using the Millstone Hill UHF Incoherent Scatter Radar System. In *Proceedings of the meteoroids 2001 conference* (pp. 457–463).

Galindo, F. R., Urbina, J., Chau, J. L., Dyrud, L., & Milla, M. (2013). On the characterization of radar receivers for meteor-head echoes studies. *Radio Science*, *48*, 33–41. doi: 10.1029/2012RS005034

Gao, B., & Mathews, J. D. (2015). High-altitude meteors and meteoroid fragmentation observed at the Jicamarca Radio Observatory. *Monthly Notices of the Royal Astronomical Society*, *446*, 3404–3415. doi: 10.1093/mnras/stu2176

Guttormsen, G., Fletcher, A. C., & Oppenheim, M. M. (2020). Atomic-Scale Simulations of Meteor Ablation. *Journal of Geophysical Research: Space Physics*, *125*. doi: 10.1029/2020JA028229

Hedges, T., Lee, N., & Elschot, S. (2022). *Meteor Head Echo Data from Concurrent Data Collect at RISR-N, JRO, and MHO* [dataset]. Zenodo. Retrieved from `https://doi.org/10.5281/zenodo.6589243` doi: 10.5281/zenodo.6589243

Janches, D., Close, S., & Fentzke, J. T. (2008). A comparison of detection sensitivity between ALTAIR and Arecibo meteor observations: Can high power and large aperture radars detect low velocity meteor head-echoes. *Icarus*, *193*, 105–111. doi: 10.1016/j.icarus.2007.08.022

Janches, D., Dyrud, L. P., Broadley, S. L., & Plane, J. M. (2009). First observation of micrometeoroid differential ablation in the atmosphere. *Geophysical Research Letters*, *36*. doi: 10.1029/2009GL037389

Kozlovsky, A., Lukianova, R., & Lester, M. (2020). Occurrence and Altitude of the Long-Lived Nonspecular Meteor Trails During Meteor Showers at High Latitudes. *Journal of Geophysical Research: Space Physics*, *125*. doi: 10.1029/2019JA027746

Li, A., & Close, S. (2015). Mean thermospheric density estimation derived from satellite constellations. *Advances in Space Research*, *56*, 1645–1657. doi: 10.1016/j.asr.2015.07.022

Li, A., & Close, S. (2016). Neutral density estimation derived from meteoroid measurements using high-power, large-aperture radar. *Journal of Geophysical Research*, *121*, 8023–8037. doi: 10.1002/2015JD024547

Li, Y., & Zhou, Q. (2019, 04). Velocity and orbital characteristics of micrometeors observed by the Arecibo 430 MHz incoherent scatter radar. *Monthly Notices of the Royal Astronomical Society*, *486*(3), 3517-3523. Retrieved from `https://doi.org/10.1093/mnras/stz1073` doi: 10.1093/mnras/stz1073

Limonta, L., Close, S., & Marshall, R. A. (2020). A technique for inferring lower thermospheric neutral density from meteoroid ablation. *Planetary and Space Science*, *180*. doi: 10.1016/j.pss.2019.104735

Loveland, R., MacDonell, A., Close, S., Oppenheim, M., & Colestock, P. (2011). Comparison of methods of determining meteoroid range rates from linear frequency modulated chirped pulses. *Radio Science*, *46*, RS2007. doi: 10.1029/2010RS004479

Marshall, R. A., Brown, P., & Close, S. (2017). Plasma distributions in meteor head echoes and implications for radar cross section interpretation. *Planetary and Space Science*, *143*, 203–208. doi: 10.1016/j.pss.2016.12.011

Marshall, R. A., & Close, S. (2015). An FDTD model of scattering from meteor head plasma. *Journal of Geophysical Research A: Space Physics*, *120*, 5931–5942. doi: 10.1002/2015JA021238

Mathews, J. D., Briczinski, S. J., Meisel, D. D., & Heinselman, C. J. (2008). Radio and meteor science outcomes from comparisons of meteor radar observations at AMISR Poker Flat, Sondrestrom, and Arecibo. *Earth, Moon and Planets*, *102*, 365–372. doi: 10.1007/s11038-007-9168-0

Matzka, J., Stolle, C., Yamazaki, Y., Bronkalla, O., & Morschhauser, A. (2021). The Geomagnetic Kp Index and Derived Indices of Geomagnetic Activity. *Space Weather*, *19*(5), e2020SW002641. doi: 10.1029/2020SW002641

Oppenheim, M. M., & Dimant, Y. S. (2015). First 3-D simulations of meteor plasma dynamics and turbulence. *Geophysical Research Letters*, *42*, 681–687. doi: 10.1002/2014GL062411

Oppenheim, M. M., Vom Endt, A. F., & Dyrud, L. P. (2000). Electrodynamics of meteor trail evolution in the equatorial E-region ionosphere. *Geophysical Research Letters*, *27*(19), 3173–3176. doi: 10.1029/1999GL000013

Popova, O., Sidneva, S., Strelkov, A., & Shuvalov, V. (2001). Formation of disturbed area around fast meteor body. *Proceedings of the Meteoroids 2001 Conference*, 237–245.

Skolnik, M. I. (2008). *Radar Handbook* (3rd ed.). New York: The McGraw-Hill Companies.

Sparks, J. J., Janches, D., Nicolls, M., & Heinselman, C. (2009). Seasonal and diurnal variability of the meteor flux at high latitudes observed using PFISR. *Journal of Atmospheric and Solar-Terrestrial Physics*, *71*, 644–652. doi: 10.1016/j.jastp.2008.08.009

Sugar, G., Marshall, R., Oppenheim, M. M., Dimant, Y. S., & Close, S. (2021). Simulation-Derived Radar Cross Sections of a New Meteor Head Plasma Distribution Model. *Journal of Geophysical Research: Space Physics*, *126*. doi: https://doi.org/10.1029/2021JA029171

Sugar, G., Oppenheim, M. M., Dimant, Y. S., & Close, S. (2018). Formation of Plasma Around a Small Meteoroid: Simulation and Theory. *Journal of Geophysical Research: Space Physics*, *123*, 4080–4093. doi: 10.1002/2018JA025265

Sugar, G., Oppenheim, M. M., Dimant, Y. S., & Close, S. (2019). Formation of Plasma Around a Small Meteoroid: Electrostatic Simulations. *Journal of Geophysical Research: Space Physics*, *124*, 3810–3826. doi: 10.1029/2018JA026434

Urbina, J., & Briczinski, S. (2011). Transmitter Power Studies on Meteor Radar Head Echo Returns. In *2011 xxxth ursi general assembly and scientific symposium, general assembly and scientific symposium.* Blackwell Publishing Ltd. doi: 10.1029/2009JA014054

Vertatschitsch, L. E., Sahr, J. D., Colestock, P., & Close, S. (2011). Meteoroid head echo polarization features studied by numerical electromagnetics modeling. *Radio Science*, *46*, RS6016. doi: 10.1029/2011RS004774

Vida, D., Brown, P. G., Campbell-Brown, M., Weryk, R. J., Stober, G., & McCormack, J. P. (2021). High precision meteor observations with the Canadian automated meteor observatory: Data reduction pipeline and application to meteoroid mechanical strength measurements. *Icarus*, *354*. doi: 10.1016/j.icarus.2020.114097

Volz, R., & Close, S. (2012). Inverse filtering of radar signals using compressed sensing with application to meteors. *Radio Science*, *47*, RS0N05. doi: 10.1029/2011RS004889